Adaptive computation for elastic wave propagation in plate/shell structures under moving loads

Bing Tie — Denis Aubry — Arnaud Boullard

Laboratoire de Mécanique Sols-Structures-Matériaux (CNRS UMR 8579),
Ecole Centrale Paris, Grande voie des vignes,
F-92295 Châtenay Malabry cedex

{tie, aubry, boullard}@mssmat.ecp.fr

ABSTRACT. *An adaptive remeshing method tailored to computations for elastic wave propagation is proposed and its application to the elastic wave propagation in plates or shells under moving loads is presented. The method is defined within the framework of the space-time discontinuous Galerkin method, which is particularly suitable for dealing with adaptive meshes that change in time. An a priori theoretical wave propagation analysis is done to determinate an appropriate element size, then the mesh adaption strategy consists of refining finite elements according to this size in zones where local unbalanced residuals are large. The plate/shell structures are modelled with Mindlin kinematics and the dispersive phenomenon of bending waves is considered. The pertinence of the Kirchhoff-Love and Mindlin kinematical models with respect to frequency ranges and plate/shell thickness is discussed. Numerical examples are given to illustrate the interest of the adaptive method.*

RÉSUMÉ. *Cet article présente une méthode adaptative dédiée à la modélisation de la propagation d'ondes élastiques et son application aux plaques et coques soumises à une charge mobile. Cette méthode utilise la technique de remaillage pour l'adaptation de maillage. Elle est dévelopée dans le cadre de la méthode de Galerkin discontinue espace-temps, qui est particulièrement appropriée pour traiter des maillages éléments finis qui changent dans le temps. Une analyse théorique a priori des ondes élastiques est faite pour déterminer une taille d'élément adéquate, puis l'adaptation de maillage consiste à raffiner les éléments finis en respectant cette taille dans les zones où les résidus locaux de déséquilibre sont grands. Les plaques ou coques sont modélisées avec le modèle cinématique de Mindlin et le phénomène dispersif des ondes de flexion est considéré. La pertinence des modèles de Mindlin et de Kirchhoff-Love est discutée. Les exemples numériques sont présentés pour illustrer l'intérêt de la méthode adaptative.*

KEYWORDS: *elastic wave propagation, adaptive remeshing method, a posteriori error estimates, space-time discontinuous Galerkin method, shell modelling.*

MOTS-CLÉS : *propagation des ondes élastiques, méthode adaptative, remaillage, estimation d'erreur a posteriori, méthode de Galerkin discontinue espace-temps, modélisation coque.*

REEF – 12/2003. Estimateurs d'erreur, pages 717 à 736

1. Introduction

Finite element modelling of elastic wave propagation in engineering structures for medium or high frequency ranges is very time and memory consuming because small finite elements and time discretization step are required to capture wave fonts. As the wave fronts move throughout the whole structure and their time-dependent pattern is generally unknown beforehand, adaptive finite element methods, capable to automatically perform mesh refinement and coarsening, naturally suggest themselves. Small finite elements are only used around the wave fronts and finite element meshes evolve in time with respect to the wave propagation phenomena.

Here, an adaptive remeshing method tailored to computations for elastic wave propagation is given. The method is defined within the framework of the space-time discontinuous Galerkin formulation, which is more accurate than the usually used Newmark scheme. Furthermore, its numerical damping allows to filter high frequency numerical noises and to give proper representation of shock wave fronts. This property has a great interest in numerical modelling of elastic waves in a structure under moving dynamic loads. Indeed, it is well known that shock waves emerge when the speed of the moving loads is higher than the velocity of wave propagation in the structure. In Figure 1, it is shown, in an one dimensional elastic structure submitted to a rectangular compression load, the capture of wave fronts by respectively the discontinuous Galerkin method and the trapezoidal Newmark scheme. It is obvious that the filtering of spurious high-frequency modes of the discontinuous Galerkin method guarantees a proper capture of the waves fronts.

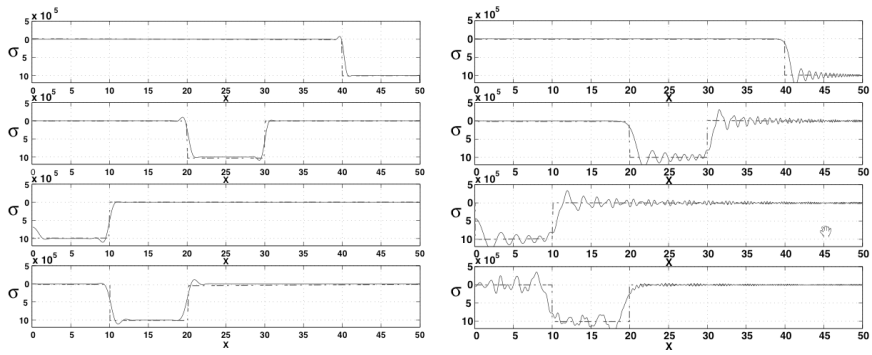

Figure 1. *Numerical capture of stresses wave fronts in a one dimensional strcuture under a rectangular compression load. Left: by discontinuous Galerkin method; Right: by the trapezoidal Newmark scheme*

As far as the mesh adaption is concerned, the discontinuous Galerkin formulation is particularly suitable to deal with adaptive meshes that change in time, for the displacement and velocity discontinuities are directly involved and treated in the

formulation. The variational framework of the discontinuous Galerkin method is also used to define *a posteriori* error estimators that investigate local unbalanced residuals. It has been shown that an upper bound of the discretization error could be obtained (Hulbert *et al.* 1988, Johnson *et al.* 1992, Aubry *et al.* 1999).

The mesh adaption, only performed in space in this work, is done by a whole remeshing of the structure according to a map of element sizes defined with respect to the *a posteriori* error estimators. Therefore, the mesh coarsening is as easy as the mesh refinement. As elastic wave propagation phenomena involve wavelength scales, the definition of the remeshing size map also takes into account the shortest wavelength related to the frequency range under study. In this work, the adaptive remeshing systematically places ten finite elements in the shortest wavelength. Furthermore, the whole remeshing technique that we have developed matches exactly the geometry of structure, that is all newly generated nodes are added exactly on the structure but not on the old finite element mesh. So, geometrical discretization by finite element mesh of shell structures is improved around wave fronts during the mesh adaption.

There are two deeper sources of difficulty peculiar to numerical modelling of elastic waves in plate or shell structures. The first one is the dispersive character of the bending waves: their propagation velocity depends upon the frequency and upon the thickness of the plate or shell. The shortest wavelength of bending waves under study decreases when the frequency increases and becomes rapidly very small in comparison with the structure characteristic dimension. The second difficulty is due to complex transmission and conversion of waves in jointed plates on joint interfaces or in shells because of the curvature. In these structures, adaptive methods is even more interesting, as the membrane and the bending waves are fully coupled, therefore very refined discretization in time and in space is required to describe unexpected propagation patterns. Due to the dispersive character of the bending waves, it is necessary to devise the suitable choice of kinematical model. Indeed, a “thin” shell under low frequency consideration becomes a “thick” shell when the frequency under study increases. Here, a first investigation of the pertinence of the Kirchhoff-Love kinematical model (for thin plates) and the Mindlin one (for thick plates) is given.

As for the numerical application of our adaptive approach, we consider plate or shell structures under moving loads, which model a kind of mechanical charges that are important in the industry. It is well known that in the supersonic regime, where the speed of the moving loads is higher then the wave propagation velocities, shock waves are generated. Our numerical examples show that the adaptive approach is very powerful to capture those shock wave fronts.

2. Mindlin shell modelling

We consider the dynamic equilibrium of a shell structure Ω. The well-known Mindlin kinematical model states that the shell's normal fibres remain straight during deformation and the displacement field in a shell is entirely determined by $\boldsymbol{u}_0$ the displacement of the shell mean surface Σ and by $\boldsymbol{u}_{1S}$ the rotation of normal fibres, $\boldsymbol{u}_{1S}$ is tangent to Σ:

$$\boldsymbol{u}(\boldsymbol{x}_0, \zeta) = \boldsymbol{u}_0(\boldsymbol{x}_0) + \zeta \boldsymbol{u}_{1S}(\boldsymbol{x}_0) \tag{1}$$

$\boldsymbol{x}_0$ denotes a point on $\Sigma$and $\zeta$the normal altitude of any point to Σ. According to (1), the infinitesimal strain tensor $\boldsymbol{\varepsilon}(\boldsymbol{u})$ reads as:

$$\begin{aligned} \boldsymbol{\varepsilon}_x(\boldsymbol{u}) &= \boldsymbol{\mu}^{-1}.(\boldsymbol{\varepsilon}_{ss}(\boldsymbol{u}) + \boldsymbol{n} \otimes_{sym} \boldsymbol{\gamma}).\boldsymbol{\mu}^{-1} \\ \boldsymbol{\gamma} &= \boldsymbol{grad}_s(u_{0n}) - \boldsymbol{b}(\boldsymbol{u}_{0s}) + \boldsymbol{u}_1 \end{aligned} \tag{2}$$

where all variables indexed by "s" are tangent to the shell mean surface Σ and all derivation operator indexed by "s" are tangent derivation operator with respect to Σ. $\boldsymbol{n}$ denoting the normal unitary vector field to Σ, $\boldsymbol{b} = D_s\boldsymbol{n}$ is the curvature tensor and $\boldsymbol{\mu} = \boldsymbol{I} + \zeta\boldsymbol{b}$. $\boldsymbol{\gamma}$ is the normal transverse shear strain. "$\otimes_{sym}$" denotes the symmetried tensor product.

The Mindlin model assumes that the transverse normal stress vanishes ($\sigma_{nn} = 0$) and utilizes a plane stress elasticity tensor, denoted by $\boldsymbol{C}$ in this paper. We decompose the Cauchy stress tensor as follows:

$$\boldsymbol{\sigma}_x = \boldsymbol{\mu}.(\boldsymbol{\sigma}_{ss} + \boldsymbol{q} \otimes \boldsymbol{n} + \boldsymbol{n} \otimes \boldsymbol{q}).\boldsymbol{\mu} \tag{3}$$

Then the principle of virtual works allows writing the following weak dynamic equilibrium equation:

$$(\rho \partial_{tt}\boldsymbol{u}, \boldsymbol{w})_\Omega + (\boldsymbol{\sigma}_x(\boldsymbol{u}), \boldsymbol{\varepsilon}_x(\boldsymbol{w}))_\Omega = (\boldsymbol{f}, \boldsymbol{w})_\Omega \quad \textit{for all } \boldsymbol{w} \in V(\Omega) \tag{4}$$

where ρ is the volumic density, $\boldsymbol{f}$ is the external volume loads, $\boldsymbol{w}$ is the Mindlin-type virtual displacement, $V(\Omega)$ is the usual space of the kinematically admissible Mindlin-type displacements, $(\bullet,\bullet)_\Omega$ denotes the integration on Ω of the usual inner products between two vector or tensor fields.

By defining the following generalized internal and external forces:

$$\begin{gathered} \boldsymbol{N}_{ss} = \int_{\mathfrak{I}} \boldsymbol{\sigma}_{ss}\, d\zeta\,,\ \boldsymbol{M}_{ss} = \int_{\mathfrak{I}} \zeta\boldsymbol{\sigma}_{ss}\, d\zeta\,,\ \boldsymbol{R}_{ss} = \int_{\mathfrak{I}} \zeta^2\boldsymbol{\sigma}_{ss}\, d\zeta\,,\ \boldsymbol{Q} = \int_{\mathfrak{I}} \boldsymbol{q}\, d\zeta \\ F_n = \int_{\mathfrak{I}} f_n\, d\zeta,\ \boldsymbol{F}_s = \int_{\mathfrak{I}} \boldsymbol{f}_s\, d\zeta\,,\ \boldsymbol{C} = \int_{\mathfrak{I}} \zeta\boldsymbol{f}_s\, d\zeta \end{gathered} \tag{5}$$

the strong equilibrium equations that governs the dynamic equilibrium of shells reads as:

$$
\begin{aligned}
(\mathbf{Div}_s(\mathbf{N}_{ss}+\mathbf{b}.\mathbf{M}_{ss}))_s + \mathbf{b}(\mathbf{Q}) + \mathbf{F}_s &= (e + J_1 det(\mathbf{b}))\rho\partial_{tt}\mathbf{u}_{0s} + J_1 tr(\mathbf{b})\ \rho\partial_{tt}\mathbf{u}_1 \\
div_s\mathbf{Q} - tr((\mathbf{N}_{ss}+\mathbf{b}.\mathbf{M}_{ss}).\mathbf{b}) + F_n &= (e + J_1 det(\mathbf{b}))\rho\partial_{tt}u_{0n} \\
(\mathbf{Div}_s(\mathbf{M}_{ss}+\mathbf{b}.\mathbf{R}_{ss}))_s - \mathbf{Q} + \mathbf{C} &= (J_1 + J_2 det(\mathbf{b}))\rho\partial_{tt}\mathbf{u}_{0s} + J_1 tr(\mathbf{b})\rho\partial_{tt}\mathbf{u}_{0s}
\end{aligned}
\tag{6}
$$

with $tr(b) = \sum_i b_{ii}$, $J_1 = e^3/12$, $J_2 = e^5/80$, e the shell thickness and $\Im$ the interval $]-e/2, e/2[$. Here for simplicity concern, the equations describing the initial and the boundary conditions are omitted.

It is obvious that, by putting $\mathbf{b} = \mathbf{0}$ in the equations (4), we get the strong dynamic equilibrium formulation of a plate. In the case where the geometry mean surface of a plate coincides with its material mean surface, it can be shown that the constitutive equations link $(\mathbf{N}_{ss}, \mathbf{u}_{0s})$ together on the one hand and $(\mathbf{M}_{ss}, \mathbf{Q}, u_{0n}, \mathbf{u}_1)$ together on the other hand. Therefore, the membrane phenomena described by the first equation are completely uncoupled with the bending phenomena governed by the others two equations. Therefore, it is the non-zero curvature of the shell that couples membrane and bending waves all together. In a structure made by assembled plates, the coupling of the membrane and bending waves is due to the wave transmission and conversion at junction interfaces, even if the membrane and bending equations are uncoupled in each individual plate.

3. Space-time discontinuous Galerkin formulation

The basic idea of the space-time discontinuous Galerkin method consists in considering the whole space-time domain $S = \Omega\times$□□□$]$ by subdividing it in space-time slabs $S_n = \Omega\times$□t_n□$t_{n+1}]$, $[0,T]$ is the whole time interval under study. The weak formulation (4) is transformed to a first order differential system and integrated over each space-time slab:

$$
\begin{aligned}
&(\rho\partial_t\mathbf{v},\ \mathbf{w}_v)_{Sn} + (\boldsymbol{\sigma}_x(\mathbf{u}),\ \boldsymbol{\varepsilon}_x(\mathbf{w}_v))_{Sn} + (\rho[\mathbf{v}(t_n)],\ \mathbf{w}_v(t_n^+))_{\Omega} = (\mathbf{f},\ \mathbf{w}_v)_{Sn} \\
&(\boldsymbol{\sigma}_x(\partial_t\mathbf{u} - \mathbf{v}),\ \boldsymbol{\varepsilon}_x(\mathbf{w}_u))_{Sn} + (\boldsymbol{\sigma}_x[\mathbf{u}(t_n)],\ \boldsymbol{\varepsilon}_x(\mathbf{w}_u(t_n^+)))_{\Omega} = 0 \\
&\qquad\qquad \text{for all } (\mathbf{w}_v,\ \mathbf{w}_u)\in V(S_n)\times V(S_n)
\end{aligned}
\tag{7}
$$

where $\mathbf{v} = \partial_t\mathbf{u}$ is the velocity field, $[\bullet(t_n)]$ denotes the jump quantities in time at the beginning of each space-time slab t_n. The discontinuous Galerkin method applied to the elastodynamics gives rise to a two fields formulation: the first equation of (7) describes the dynamic equilibrium and the second one is the compatibility condition between displacement and velocity fields.

As for the finite element discretization of each space-time slab, we utilise only one linear finite element in time and a free finite element mesh in space, that is:

$$\boldsymbol{u}_{\Delta t,h}(t) = ((t_{n+1}-t)/\Delta t)\ \boldsymbol{U}_n + ((t - t_n)/\Delta t)\ \boldsymbol{U}_{n+1}$$
$$\boldsymbol{v}_{\Delta t,h}(t) = ((t_{n+1}-t)/\Delta t)\ \boldsymbol{V}_n + ((t - t_n)/\Delta t)\ \boldsymbol{V}_{n+1} \qquad (8)$$

where $\Delta t = t_{n+1} - t_n$, $(\boldsymbol{U}_n, \boldsymbol{U}_{n+1}, \boldsymbol{V}_n, \boldsymbol{V}_{n+1})$ are respectively the finite element solutions of $(\boldsymbol{u}(t_n^+), \boldsymbol{u}(t_{n+1}^-), \boldsymbol{v}(t_n^+), \boldsymbol{v}(t_{n+1}^-))$. When the discretization (8) is plugged in the weak form (7), a system of linear equations (9) for the unknown $\boldsymbol{V}_n$ and $\boldsymbol{V}_{n+1}$ is obtained and is solved iteratively (Wiberg *et al.* 1998):

$$\begin{aligned}
&(\rho \boldsymbol{V}_n, \boldsymbol{W})_\Omega + (\Delta t^2/6)(\boldsymbol{\sigma}_x(\boldsymbol{V}_n), \boldsymbol{\varepsilon}_x(\boldsymbol{W}))_\Omega + (2/3)(\rho \boldsymbol{V}_{n+1}, \boldsymbol{W})_\Omega \\
&= ((\Delta t/2)\boldsymbol{f}_n - (\Delta t/6)\boldsymbol{f}_{n+1}, \boldsymbol{W})_\Omega + (5/3)(\rho \boldsymbol{V}_n^-, \boldsymbol{W})_\Omega - (2\Delta t/3)(\boldsymbol{\sigma}_x(\boldsymbol{U}_n^-), \boldsymbol{\varepsilon}_x(\boldsymbol{W}))_\Omega \\
&(\rho \boldsymbol{V}_{n+1}, \boldsymbol{W})_\Omega + (\Delta t^2/6)(\boldsymbol{\sigma}_x(\boldsymbol{V}_{n+1}), \boldsymbol{\varepsilon}_x(\boldsymbol{W}))_\Omega + (\Delta t^2/3)(\boldsymbol{\sigma}_x(\boldsymbol{V}_n), \boldsymbol{\varepsilon}_x(\boldsymbol{W}))_\Omega \\
&= (\Delta t/2)(\boldsymbol{f}_n + \boldsymbol{f}_{n+1}, \boldsymbol{W})_\Omega + (\rho \boldsymbol{V}_n^-, \boldsymbol{W})_\Omega - \Delta t(\boldsymbol{\sigma}_x(\boldsymbol{U}_n^-), \boldsymbol{\varepsilon}_x(\boldsymbol{W}))_\Omega
\end{aligned} \qquad (9)$$

The iterative solver is in fact the bloc Jacobi method: the diagonal dynamic matrix is factorized while the extra-diagonal coupling terms are putted into the second members. The unconditional convergence of this iterative solver has been shown (Leclère 2001).

The velocity unknowns $\boldsymbol{V}_n$ and $\boldsymbol{V}_{n+1}$ being solved, then the displacement unknowns $\boldsymbol{U}_n$ and $\boldsymbol{U}_{n+1}$ are simply updated using (10). The discontinuous Galerkin scheme is implicit in the sense that it requires the inversion of a dynamic matrix involving the stiffness matrix. The number of unknowns is also doubled in comparison to the classical finite difference schemes. Furthermore when the adaptive remeshing is performed, the update of the displacement fields (10) requires solving a linear system. So, the discontinuous Galerkin scheme is more time and memory consuming than the Newmark scheme.

$$\begin{aligned}
(\boldsymbol{\sigma}_x(\boldsymbol{U}_n), \boldsymbol{\varepsilon}_x(\boldsymbol{W}))_\Omega &= (\boldsymbol{\sigma}_x(\boldsymbol{U}_n^-), \boldsymbol{\varepsilon}_x(\boldsymbol{W}))_\Omega - (\Delta t/6)(\boldsymbol{\sigma}_x(\boldsymbol{V}_{n+1} - \boldsymbol{V}_n), \boldsymbol{\varepsilon}_x(\boldsymbol{W}))_\Omega \\
(\boldsymbol{\sigma}_x(\boldsymbol{U}_{n+1}), \boldsymbol{\varepsilon}_x(\boldsymbol{W}))_\Omega &= (\boldsymbol{\sigma}_x(\boldsymbol{U}_n^-), \boldsymbol{\varepsilon}_x(\boldsymbol{W}))_\Omega + (\Delta t/2)(\boldsymbol{\sigma}_x(\boldsymbol{V}_{n+1} + \boldsymbol{V}_n), \boldsymbol{\varepsilon}_x(\boldsymbol{W}))_\Omega
\end{aligned} \qquad (10)$$

A principal contribution of the discontinuous Galerkin method resides in the fact that the continuity of the unknown fields is not necessary and the discontinuities are directly involved and treated in the weak formulation within appropriate inner products. In our case, the displacement and the velocity can be discontinuous from one space-time slab to the sequent one and the energy dissipated by displacement and velocity jumps are controlled by the terms $(\rho[\boldsymbol{v}(t_n)], \boldsymbol{w}_v(t_n^+))_\Omega$and $(\boldsymbol{\sigma}_x([\boldsymbol{u}(t_n)]), \boldsymbol{\varepsilon}_x(\boldsymbol{w}_u(t_n^+)))_\Omega$.It has been shown that the unconditional stability of the space-time discontinuous Galerkin formulation is guaranteed thanks to these discontinuity terms (Leclère 2001). This is extremely important within the frameworks of the free mesh adaption according to the wave propagation phenomena. It is obvious that a time

integration scheme with an explicit stability condition should be very difficult to manage when adaptive meshes change in time and constitutes an obstacle to successfully perform adaptive computation.

Another difficulty to perform adaptive remeshing with a classical finite difference scheme such as the Newmark one is to properly interpolate the displacement and velocity fields from the mesh of the preceding time step on the one of the current time step. Indeed, even if the time integration scheme is unconditionally stable, the energy of whole dynamic system may not be conserved if the interpolation is done using an unsuitable inner product. Thanks to the jump terms in the discontinuous Galerkin formulations, the interpolation of mechanical fields between adaptive meshes is straightforward: The velocity field $\boldsymbol{V}_n^-$ and the displacement field $\boldsymbol{U}_n^-$ defined on the mesh M^- of the space-time slab $[t_{n-1}^+, t_n^-]$ are projected on the virtual field $\boldsymbol{W}$ defined on the mesh M^+ of the space-time slab $[t_n^+, t_{n+1}^-]$ using respectively the inner product $(\rho \boldsymbol{V}_n^-, \boldsymbol{W})_\Omega$ of kinetic energy and the one $(\boldsymbol{\sigma}_x(\boldsymbol{U}_n^-), \boldsymbol{\varepsilon}_x(\boldsymbol{W}))_\Omega$ of elastic energy. As the mesh adaption is made by a whole remeshing of the structure with free meshes during transient computation, the meshes M^+ and M^- do not match at all. The calculation of the inner products $(\rho \boldsymbol{V}_n^-, \boldsymbol{W})_\Omega$ and $(\boldsymbol{\sigma}_x(\boldsymbol{U}_n^-), \boldsymbol{\varepsilon}_x(\boldsymbol{W}))_\Omega$ is done using the Gaussian quadrature on the mesh M^+. At each integration point of M^+, values of the fields $\boldsymbol{V}_n^-$ and $\boldsymbol{\sigma}_x(\boldsymbol{U}_n^-)$ can be obtained with the finite element interpolation on the mesh M^-. It is obvious that, in such a way, numerical errors are added in our finite element modelling. In order to minimize this error, the strategy adopted in this work consists in using a Gaussian quadrature rule of high order when evaluating the terms $(\rho \boldsymbol{V}_n^-, \boldsymbol{W})_\Omega$ and $(\boldsymbol{\sigma}_x(\boldsymbol{U}_n^-), \boldsymbol{\varepsilon}_x(\boldsymbol{W}))_\Omega$. For numerical examples presented hereafter, seven Gauss points per element are used for those numerical integrations.

4. A posteriori error analysis and adaptive computation

Several classes of methods for the *a posteriori* error estimates have been developed in the literature, namely the so-called Z^2-method proposed by Zienkiewicz and Zhu based on the post stress smoothing processes (Zienkiewicz *et al.* 1992), the Ladevèze's method that explicitly builds static admissible stress fields (Ladevèze 1983) and the residual forces method, which investigates the unbalanced residuals using enriched finite elements bases (Babuska *et al.* 1978, Bank *et al.* 1992, Oden *et al.* 1989, Tie 1993).

4.1. *Dynamic unbalanced residuals for the discontinuous Galerkin formulation*

In this work, the residual forces method is used. The dynamic unbalanced residuals are defined when the finite element space-time solutions $(\boldsymbol{u}_{\Delta t,h}, \boldsymbol{v}_{\Delta t,h})$ are injected in the exact space-time Galerkin weak formulation (7):

$$R_{eq}(\boldsymbol{w}_v)_{Sn} = (\boldsymbol{f}, \boldsymbol{w}_v)_{Sn} - (\rho \partial_t \boldsymbol{v}_{\Delta t,h}, \boldsymbol{w}_v)_{Sn} - (\boldsymbol{\sigma}_x(\boldsymbol{u}_{\Delta t,h}), \boldsymbol{\varepsilon}_x(\boldsymbol{w}_v))_{Sn}$$

$$- (\rho[\boldsymbol{v}_{\Delta t,h}(t_n)],\ \boldsymbol{w}_v(t_n^+))_\Omega$$

$$R_c(\boldsymbol{w}_u)_{Sn} = - (\boldsymbol{\sigma}_x(\partial_t \boldsymbol{u}_{\Delta t,h} - \boldsymbol{v}),\ \boldsymbol{\varepsilon}_x(\boldsymbol{w}_u))_{Sn} - (\boldsymbol{\sigma}_x[\boldsymbol{u}_{\Delta t,h}(t_n)],\ \boldsymbol{\varepsilon}_x(\boldsymbol{w}_u(t_n^+)))_\Omega \quad (11)$$

The first residual operator $R_{eq}(\bullet)_{Sn}$ involves in fact local dynamic unbalanced quantities such as $(\boldsymbol{f} - \rho\partial_t \boldsymbol{v}_{\Delta t,h} + \boldsymbol{Div}_x \boldsymbol{\sigma}_x(\boldsymbol{u}_{\Delta t,h}))$ in each finite element and spatial jumps in stress vector $[\boldsymbol{\sigma}_x(\boldsymbol{u}_{\Delta t,h}).\boldsymbol{n}_x]$ at the interface of finite elements. The compatibility condition between the displacement derivative and the velocity $(\partial_t \boldsymbol{u}_{\Delta t,h} - \boldsymbol{v})$, which in the context of finite differences would be considered as truncation error, is treated here as a kind of residuals by the second residual operator $R_c(\bullet)_{Sn}$. Otherwise, the time discontinuities at the beginning of the space-time slab $([\boldsymbol{v}_{\Delta t,h}(t_n)]$ and $[\boldsymbol{u}_{\Delta t,h}(t_n)])$ contribute also to both residual operators.

The discretization errors $\boldsymbol{e}_u = \boldsymbol{u} - \boldsymbol{u}_{\Delta t,h}$ and $\boldsymbol{e}_v = \boldsymbol{v} - \boldsymbol{v}_{\Delta t,h}$ are solutions of the following residuals problem:

$$(\rho\partial_t \boldsymbol{e}_v,\ \boldsymbol{w}_v)_{Sn} + (\boldsymbol{\sigma}_x(\boldsymbol{e}_u),\ \boldsymbol{\varepsilon}_x(\boldsymbol{w}_v))_{Sn} + (\rho[\boldsymbol{e}_v(t_n)],\ \boldsymbol{w}_v(t_n^+))_\Omega = R_{eq}(\boldsymbol{w}_v)_{Sn}$$

$$(\boldsymbol{\sigma}_x(\partial_t \boldsymbol{e}_u - \boldsymbol{e}_v),\ \boldsymbol{\varepsilon}_x(\boldsymbol{w}_u))_{Sn} + (\boldsymbol{\sigma}_x[\boldsymbol{e}_u(t_n)],\ \boldsymbol{\varepsilon}_x(\boldsymbol{w}_u(t_n^+)))_\Omega = R_c(\boldsymbol{w}_u)_{Sn}$$

$$for\ all\ (\boldsymbol{w}_v,\ \boldsymbol{w}_u) \in V(S_n) \times V(S_n) \quad (12)$$

It has been shown that the definition of this residual problem together with the use of the adjoin state representation of the error gives an upper bound of the error by the norm of the residuals weighted by some power of the discretization parameters $(\Delta t,\ h)$ (Hulbert *et al.* 1988, Johnson *et al.* 1992, Aubry *et al.* 1999). Therefore, an adaptive strategy that aims to decrease the discretization errors and to improve the accuracy in the wave front capture can be designed in such a way that finite elements having large local residuals are automatically refined. Now let us see how such a strategy can be actually implemented.

4.2. *A posteriori error indicators*

First of all, it is necessary to evaluate the local residuals. A common strategy to do this consists in solving residual problem (12) in a finite element space richer than $V_{\Delta t,h}(S_n)$. In order to warranty a good performance when the residuals are checked out, the residual problem is not exactly solved and only an estimated solution of $(\boldsymbol{e}_u, \boldsymbol{e}_u)$ is obtained in a local way using small patches of finite elements. There are several strategies to choose the enriched finite element space and to define the local patches (Babuska *et al.* 1978, Oden *et al.* 1989, Tie 1993).

To get enriched finite element space, the initial mesh in the space-time slab S_n can be refined in space as well as in time. But in this work the mesh adaption is only performed in space, so we need only a spatial finite element space richer than $V_h(\Omega)$. We use the uniformly refined spatial mesh $M_{h/2}$ of the initial spatial M_h to define the local patches, which are in fact groups of elements of $M_{h/2}$ surrounding each extra

node introduced by $M_{h/2}$ (Tie 1993, Aubry *et al.* 1997). We note that, not as the local patches, the uniformly refined mesh $M_{h/2}$ is never actually built. The residual problem (12) is solved on each patch with homogeneous Dirichlet boundary conditions. The local error solutions $(\boldsymbol{e}_u^*, \boldsymbol{e}_u^*)$ on each patch $\wp$ are measured within the kinetic and elastic norms:

$$(1/2)(\rho \boldsymbol{e}_v^*, \boldsymbol{e}_v^*)_{\wp \times \Delta t} + (1/2)(\boldsymbol{\sigma}_x(\boldsymbol{e}_u^*), \boldsymbol{\varepsilon}_x(\boldsymbol{e}_u^*))_{\wp \times \Delta t} \tag{13}$$

The same strategy can be used to obtain error indicators in time: The initial time step is subdivided in two sub steps, the residual problem is then iteratively solved using the dynamic matrix already calculated in the initial space-time slab. It has been shown that few iterations are sufficient to produce good time error indicators (Leclère 2001).

4.3. *Adaptive remeshing strategy*

The adaptive remeshing is driven by the local error indicators (13): The comparison of the amount of local error indicators with respect to a user prescribed threshold first tells whether the mesh adaption should be performed or not. In the former case, the map of the errors is then used to define a map of element sizes for building a nearly optimal new mesh, according to the principle of the equi-distribution of error. This means that a nearly homogeneous error distribution is achieved over all the elements on the new mesh. Otherwise, to define the finite element size map, the convergence rates with respect to the element size - linear and quadratic convergences for respectively linear and quadratic elements - given by the classical finite element analyses are assumed.

As elastic wave propagation phenomena involve wavelength scales, the definition of the remeshing size map also takes into account the shortest wavelength $\lambda_{min}(f_{max})$ related to the highest frequency under study f_{max}. In this work, the adaptive remeshing systematically places at most ten elements within the shortest wavelength. When only membrane waves are considered, as the shear waves propagate more slowly than the pressure waves: $c_s < c_p$, we have:

$$\lambda_{min} = c_s/f_{max},\ h_{min} = \lambda_{min}/10,\ \Delta t = h_{min}/c_p \tag{14}$$

As far as the bending waves are concerned, the *a priori* theoretical wave analysis is necessary to find the dispersion equation, because the propagation velocity c_f of the bending waves depends upon the frequency. In the case of the Mindlin plate modelling, this dispersion equation can be explicitly written:

$$(c_f/c_s)^2 = \left|((\alpha^2-1)^2 + 4\kappa^2\alpha^2)^{1/2} - (\alpha^2 + 1)\right| / 2\left|\kappa^2-1\right| \tag{15}$$

where $\alpha = c_p/c_s$, $\kappa = (3^{1/2}/\pi)\ \lambda_s/e = (3^{1/2}/\pi)\ c_s/(f\ e)$. As $\lambda_f/\lambda_s = c_f/c_s < 1$, the shortest wavelength is given by the bending waves and depends not only upon the frequency f but also upon the plate thickness e. For the same highest frequency under study f_{max}, the thinner is the plate, the smaller should be the finite elements.

$$\lambda_{min} = c_f/f_{max}\ ,\ h_{min} = \lambda_{min}/10,\ \Delta t = h_{min}/c_p \tag{16}$$

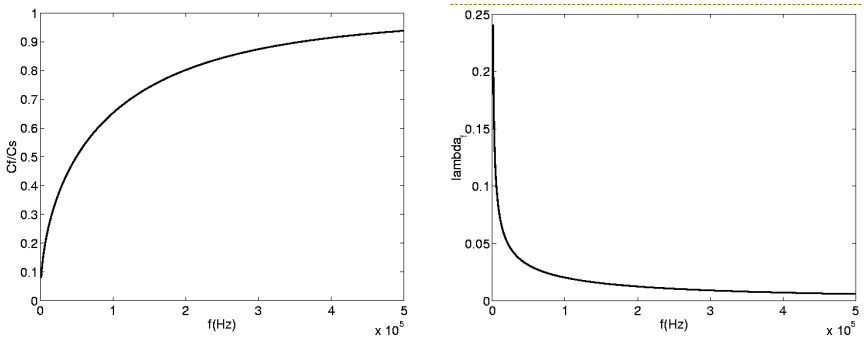

a b

Figure 2. *a) dispersion curve of bending waves, (c_f/c_s) vs. frequency; b) bending wavelength λ_f vs. frequency*

In the case of shells having any form, no analytical explicit dispersion equation like (15) is available. In this work, the discretization parameters (Δt, h_{min}) defined from the Mindlin plates are simply applied to the shell modelling.

Our adaptive remeshing strategy can be summarized as follows: zones where the wave fronts pass through are detected by the local error indicators, then finite elements of the appropriate smallest size h_{min} coming from *a priori* theoretical wave analysis are put in these zones.

4.4. *Geometric error in shell representation by finite element meshes*

The adaptive remeshing technique that we have developed respects exactly the geometry of the shells, in the sense that all newly generated nodes are added exactly on the shells but not on the old finite element mesh. So, geometrical discretization by finite element mesh of shells is improved around wave fronts during the mesh adaption.

For the geometric error in shell representation by finite element meshes, it is implicitly taken into account by the residuals (11). Indeed in the case of the shell modelling, the exact solutions ($\boldsymbol{u}$, $\boldsymbol{v}$) are defined on the true shell domain, whose geometry representation reads as:

$$\boldsymbol{\phi}(\xi, \zeta) = \boldsymbol{x}(\xi, \zeta) = \boldsymbol{x}_0(\xi) + \zeta \boldsymbol{n}(\boldsymbol{x}_0(\xi)) \tag{17}$$

where $\boldsymbol{x}_0(\xi)$ is the geometric representation of the shell mean surface Σ and $\boldsymbol{n}(\boldsymbol{x}_0(\xi))$ is the field of unitary normal-to-Σ vectors; while the finite element solution $(\boldsymbol{u}_{\Delta t,h}, \boldsymbol{v}_{\Delta t,h})$ is defined on some mesh M_h, a geometrical approximation of the shell:

$$\boldsymbol{\phi}_h(\xi, \zeta) = \boldsymbol{x}_h(\xi, \zeta) = \sum_A w_A(\xi) (\boldsymbol{x}_0(\xi_A) + \zeta \boldsymbol{n}_h(\xi_A)) \quad \textit{in each finite element } E \tag{18}$$

with $\boldsymbol{n}_h(\xi_A)$ the approximated unitary normal vector to the shell at any node A of the mesh M_h. As the residuals (11) is defined on the true shell domain, $(\boldsymbol{u}_{\Delta t,h}, \boldsymbol{v}_{\Delta t,h})$ are projected on the true shell domain using the following equation:

$$\boldsymbol{u}_{\Delta t,h}^{*}(\boldsymbol{\phi}(\xi, \zeta)) = \boldsymbol{u}_{\Delta t,h}(\boldsymbol{\phi}_h(\xi, \zeta)), \ \boldsymbol{v}_{\Delta t,h}^{*}(\boldsymbol{\phi}(\xi, \zeta)) = \boldsymbol{v}_{\Delta t,h}(\boldsymbol{\phi}_h(\xi, \zeta)) \tag{19}$$

We get finally the derivatives of $\boldsymbol{u}^{M_h}*$ with respect to $\boldsymbol{x}$:

$$\boldsymbol{D}_x(\boldsymbol{u}_{\Delta t,h}^{*}) = \boldsymbol{D}_{x^h}(\boldsymbol{u}_{\Delta t,h}).\boldsymbol{D}_\xi\boldsymbol{\phi}_h.(\boldsymbol{D}_\xi\boldsymbol{\phi})^{-1} \tag{20}$$

Therefore geometric errors made by the finite mesh on the shell geometry are taken into account by terms such as $\boldsymbol{D}_\xi\boldsymbol{\phi}_h.(\boldsymbol{D}_\xi\boldsymbol{\phi})^{-1}$ in the residuals. It is obvious that in the plate case, we have $\boldsymbol{D}_\xi\boldsymbol{\phi}_h = \boldsymbol{D}_\xi\boldsymbol{\phi}$, there is no error in representing plate geometry by any finite element mesh. As the residual problem will be solved on the local patches of the refined mesh $M_{h/2}$, the term related to the geometry representation in (20) becomes $\boldsymbol{D}_\xi\boldsymbol{\phi}_h.(\boldsymbol{D}_\xi\boldsymbol{\phi}_{h/2})^{-1}$. Hence, the local patches should be built with respect to the shell geometry if we desire to estimate the geometric errors related to the shell geometry, otherwise, we should have $\boldsymbol{D}_\xi\boldsymbol{\phi}_h = \boldsymbol{D}_\xi\boldsymbol{\phi}_{h/2}$ (See Figure 3).

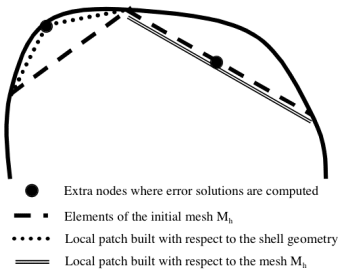

Figure 3. *Two possibilities for defining the local patches (1D-illustration)*

5. Adaptive numerical examples

Three numerical examples are presented here to illustrate the efficiency of our adaptive approach. Plates or shells in these examples are all submitted to moving loads. When the velocity of moving loads is higher than the one of wave propagation

in elastic medium, it is well known that shock waves (or head waves) are generated and usually observed in the form of a Mach cone (Eringen 1975, Ladislav Fryba 1989). Velocities and stresses are highly concentrated in shock wave fronts that are important to detect in engineering structures. The following examples illustrate how the adaptive remeshing strategy is efficient to detect and follow up these zones.

5.1. *Membrane wave propagation in a rectangular plate under moving loads*

This example considers the generation of shock waves in a membrane plate. The moving load, having a Ricker-signal type distribution in space and in time, is applied on the bottom boundary of the plate and moves with the propagation velocity of the membrane pressure wave (P-waves). We are therefore in a transonic regime, as $c_s < v = c_p$. In Figure 4, the membrane P-waves are shown with blue coloured iso-surfaces and the membrane shear waves (S-waves) with red-yellow coloured iso-surfaces. From left to right on the plate, Mach cones of respectively the P-waves and the S-waves are generated. Behind the S-waves, a small concentration zone is also observed that is due to the surface Rayleigh waves. The adaptive remeshing performs appropriate mesh refining and coarsening, which respect the wave propagation phenomena.

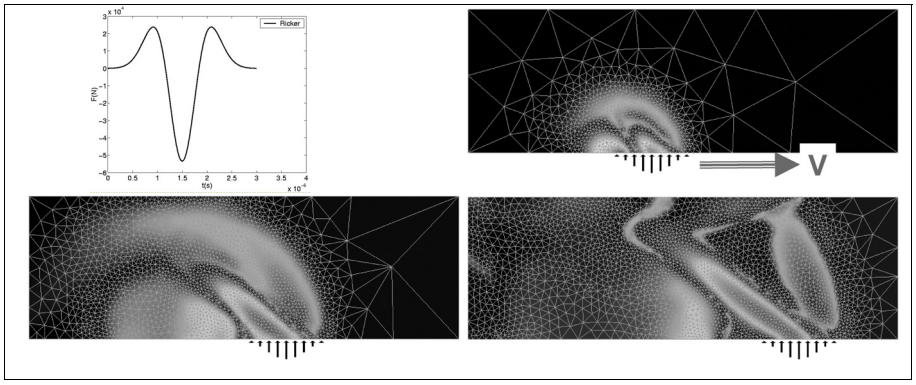

Figure 4. *Membrane wave propagation in a plate under moving loads (transonic regime, $c_s < v = c_p$). Are presented: P-waves (blue) and S-waves (red-yellow) on adaptive meshes for three time steps*

5.2. *Bending wave propagation in a rectangular plate under moving loads*

Here, we consider the propagation of bending waves in a rectangular plate. The bending load is applied on the left boundary of the plate and moves from the bottom to the top with a speed 1.3 times the P-wave's one, so much faster than the bending waves. The moving load has a very large frequency range until 100kHz, very small

finite elements are necessary to correctly model the propagation phenomena. Figure 5 shows the velocity iso-surfaces and the adaptive meshes. It is interesting to underline the dispersive character of the bending waves: wave fronts get wider in their propagation and higher frequency components propagate more rapidly than the lower frequency components.

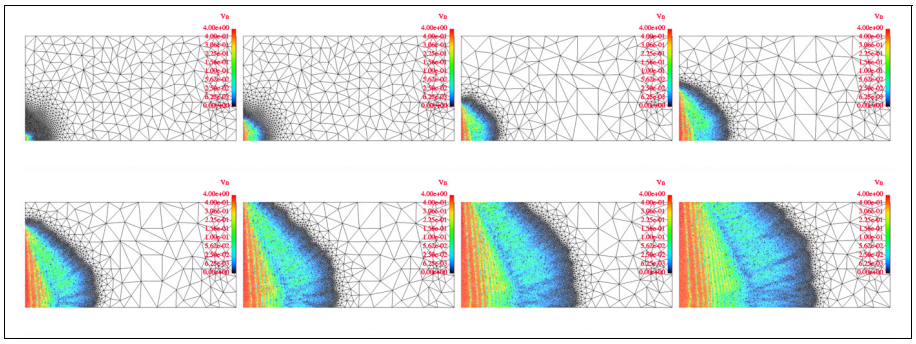

Figure 5. *Bending wave propagation in a rectangular plate. Are presented: bending velocity iso-surfaces and adaptive meshes for several time steps*

5.3. *Membrane and bending wave propagation in a cone under moving loads*

In shell structures, membrane and bending waves are fully coupled due to the curvature and conversion between them constantly occurs. Here, we are interested in modelling the wave propagation in a cone under a moving load that displaces at the cone's basis and is applied in the direction parallel to the cone's axis.

The shape of the moving load in space and in time is of Ricker signal type (see Figure 4). We are in the supersonic regime, the propagation speed of P-wave in the cone is 5000m/s while the speed of the moving load is 7000m/s. Otherwise, on the cone, there are several small rectangular zones of increased-thickness (*10* times the cone's normal thickness). Due to the continuous conversion between the membrane and bending waves, the bending wave fronts move with the same speed than the membrane wave fronts, even if the propagation velocity of bending wave is much smaller than the one of membrane waves. The larger thickness zones having a large bending inertia filter the bending waves. Membrane pressure, membrane shear and bending shock waves are observed. Once more, the efficiency of the adaptive approach is illustrated.

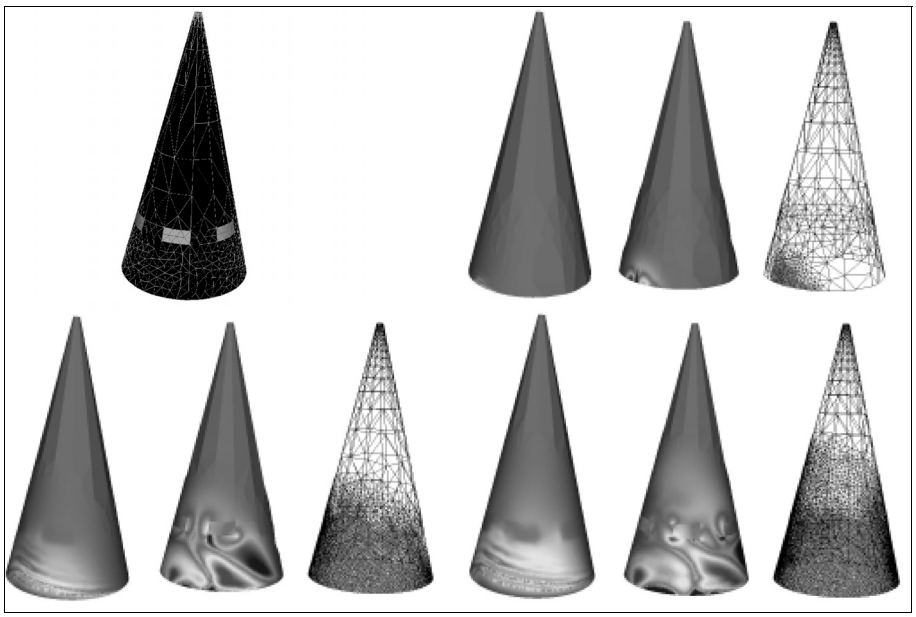

Figure 6. *Membrane and bending wave propagation in a cone, from left too right: initial mesh and increased-thickness zones; then each group of three figures presents one time step, in each group are presented bending waves, membrane P-waves (blue colour) and S-waves (red-yellow colours) and adaptive mesh*

6. Thin shell or thick shell or 3D structure?

To ensure the quality in the numerical modelling of the wave propagation phenomena, finite element size is not the only discretization parameter to control. Kinematical model used to perform shell modelling is of high importance too. In static shell modelling, according to the slenderness of the shell - the ratio between the structure characteristic dimension and the shell's thickness - the Kirchhoff-Love model for thin shells or the Mindlin one for thick shells can be used. Sometimes, 3D modelling is necessary to correctly describe localized mechanical phenomena (Aubry *et al.* 2003).

For the transient wave propagation modelling, the shell's slenderness is no more sufficient as a criterion to decide between different kinematical models, as the shell thickness should be compared to wavelengths under study. Intuitively, a geometrically thin shell would be considered as a thick shell or even a 3D structure when high frequencies intervene.

In this work, we give a first investigation of the pertinence of shell kinematical models, which is based on the theoretical wave analyses. As explicit formula are

available for the theoretical wave analyses in plates, only plates are considered here. Further studies for shells will be done in the future.

6.1. *Kirchhoff-Love plate or Mindlin plate?*

The propagation velocity of bending waves predicted by the Kirchhoff-Love model is different from the one coming from the Mindlin model (see equation (15)):

$$(c_f/c_s)^2 = 1/(\alpha\,\kappa) \tag{21}$$

We recall that $\alpha = c_p/c_s$, $\kappa = (3^{1/2}/\pi)\,\lambda_s/e = (3^{1/2}/\pi)\,c_s/(f\,e)$. According to the dispersion relation, c_f increases while λ_f the bending wavelength decreases when the frequency f increases. It is important to point out that the two dispersion relations (15) and (21) show the dependence of c_f upon the parameter κ. As κ has the same dependency with regard to the frequency f and the plate thickness e, the same bending wave propagation velocity can be obtained in a thin plate in the high frequency range or in a thick plate in the low frequency range. Therefore, in this work, when we mention that some frequency range is high or low, it is always related to the thickness of plates or shells.

The dispersion relations of the Kirchhoff-Love and the Mindlin models coincide in low frequency range but become quite different for high frequencies (see Figure 7(a)). To check the gap between these models, numerical analysis has been carried out with an academic example: the problem of the point impact of a plate. A theoretical solution is available for this problem for Kirchhoff-Love plates (Doyle 1997). To do this, we consider a square plate submitted to a point impact at its centre. The impact load is a Ricker signal with a period of 3μs. Numerical solutions are computed with the Mindlin model and are compared to the theoretical Kirchhoff-Love solutions. Only bending phenomena are modelled, as they are completely uncoupled to the membrane phenomena.

In this work, we propose to use parameter $\beta = \lambda_{f,min}/e$ - the ration between the shortest bending wavelength $\lambda_{f,min}$ intervening in the propagation and the plate thickness e - to parameterize the gap between the two models. The frequency range under study remains unchanged for the impact load is the same, a series of plates are modelled whose width is chosen such that the fastest bending wave need 1.15μs to propagate to touch the plate boundaries. Figure 8 shows that the gap between the two models becomes large when the parameter β decreases, that is the plate thickness becomes large in comparison with the shortest wavelength. For each fixed value of β, a valid frequency domain that is appropriate to the Kirchhoff-Love modelling is obtained (Figure 9). Valid frequency ranges get narrower when the plate thickness increases. In our analyses, the value *4* for the parameter β seems to be a limiting value.

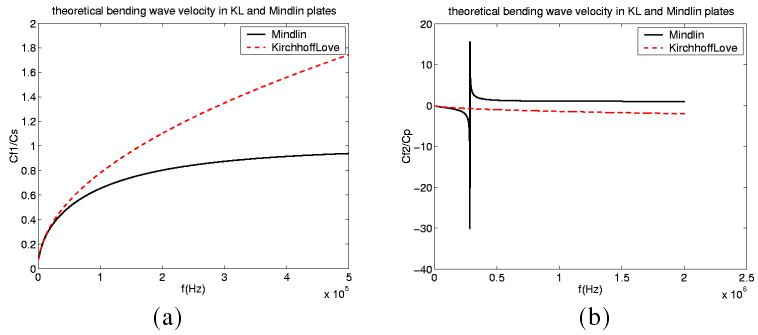

Figure 7. *Theoretical bending wave propagation velocity in Kirchhoff-Love and Mindlin plates: (a) propagative waves; (b) evanescent waves in Kirchhoff-Love plates, evanescent and propagative waves in Mindlin plates, (the "velocity" of the evanescent wave is presented as a negative value)*

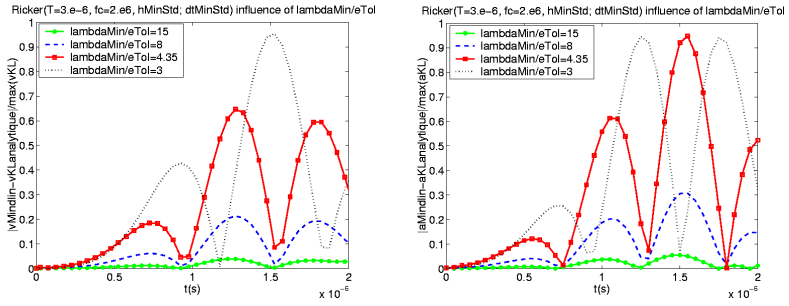

Figure 8. *Gap in velocity and in acceleration at the loading points between the theoretical Kirchhoff-Love solution and the finite element Mindlin solution in square plates with different thicknesses*

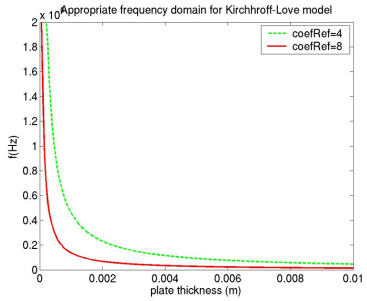

Figure 9. *Valid frequency domain of the Kirchhoff-Love model (under curves) parameterized by the ratio* $\beta = \lambda_{f,min}/e$ *(respectively equal to 4 and 8 here): on the abscissa axis is the plate thickness and on the coordinate axis is the frequency*

6.2. *Mindlin plate or 3D structure?*

The preceding paragraph has shown that thick plates or shells should be modelled by the Mindlin kinematics rather than the Kirchhoff-Love one. Now, the question is when it is necessary to perform a full 3D analysis? Is it possible to use the parameter $\beta = \lambda_{f,min}/e$ to decide either Mindlin model or 3D model should be used? Furthermore, the theoretical wave analysis of Mindlin plates gives another dispersive relation related to a bending mode that is evanescent for low frequencies (corresponding to $\kappa > 1$) and propagative for high frequencies (corresponding to $\kappa < 1$) (Figure 7(b)). These two frequency range is separated by the frequency $f_{\kappa=1}$ corresponding to $\kappa = 1$. Obviously, $f_{\kappa=1}$ depends upon the thickness of plate. When this mode is propagative, its propagation speed is larger than c_p the one of the membrane P-waves and tends to infinity when f tends to $f_{\kappa=1}$. Hence, the pertinence of the Mindlin model for the frequencies near to $f_{\kappa=1}$ should be considered.

To investigate these questions, we keep considering the academic example of the point impact problem of a plate. Numerical Mindlin and 3D solutions are carried out and compared at three points: the loading point F, the corner point S and the middle point R between F and S. Two plates are considered with β respectively equal to *3* and *0.74*. As for the previously presented examples, the width of plates is chosen such that the most rapid bending wave need 1.15μs to propagate to touch the plate boundaries. The slenderness of the two plates is respectively *6.86* and *1.55*, in usual sense, these two plates can be considered as very thick.

The highest frequency contained in the impact load is $f_{max} = 2\ 10^6 Hz$, for the plate with $\beta = 3$, we have $f_{\kappa=1} = 4.8\ 10^6 Hz$ and for the plate with $\beta = 0.74$, we have $f_{\kappa=1} = 0.85\ 10^6 Hz$. But differences observed between the Mindlin and 3D solutions for the two plates are more or less the same. The fact that the considered frequency range contains the frequency $f_{\kappa=1}$ for the plate with $\beta = 0.74$ seems has no significant effect here. In this sense, the parameter β is not a relevant parameter to decide between the Mindlin and the 3D kinematics. When reflected waves arrive at the sample points, the gap between the Mindlin and 3D solutions gets larger, this is probably due to boundary effects, which is not taken into account in our theoretical wave analyses. Further studies should be carried out.

The gap in amplitudes of acceleration is small, the Mindlin modelling predict amplitudes slightly larger than those obtained by the 3D modelling. After the arrival of the reflected waves, the gap between these two types of modelling is essentially in the wave phases. For the plate with $\beta = 0.74$, computations on two times coarsening plate and 3D meshes have been also carried out, the 3D modelling seems to be more sensitive to the mesh fineness than the Mindlin modelling. As conclusion, this first investigation seems to give some degree of confidence to the Mindlin shell modelling. This is interesting as far as the 3D modelling is much more expensive than the shell modelling and is usual impossible in engineering structures. For example, in the plate with $\beta = 0.74$, an appropriate finite mesh should approximately use 13 finite elements in the plate thickness.

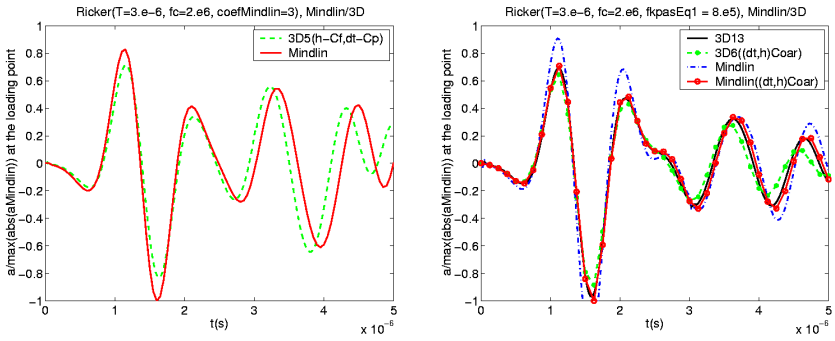

Figure 10. *Comparison of accelerations of Mindlin and 3D solutions at point F in the plates with $\beta = 3$ and $\beta = 0.74$, the arrival of the reflected waves is at 2.3 μs*

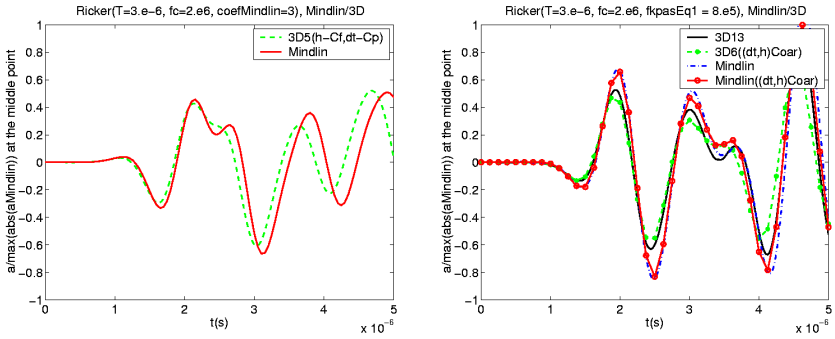

Figure 11. *Comparison of accelerations of Mindlin and 3D solutions at point R in the plates with $\beta = 3$ and $\beta = 0.74$, the arrival of the reflected waves is at 1.73 μs*

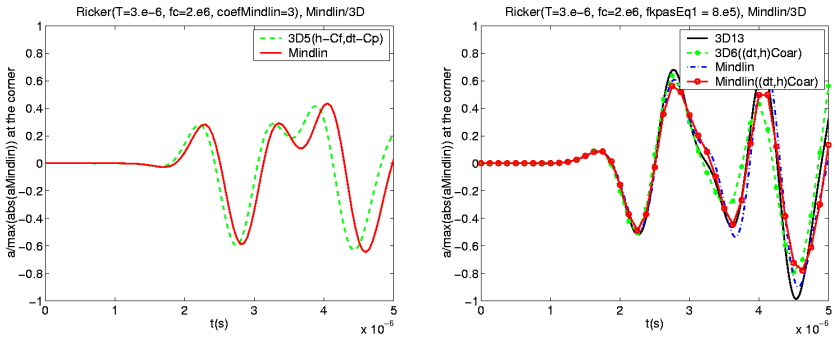

Figure 12. *Comparison of accelerations of Mindlin and 3D solutions at point S in the plates with $\beta = 3$ and $\beta = 0.74$, the arrival of the reflected waves is at 1.2 μs*

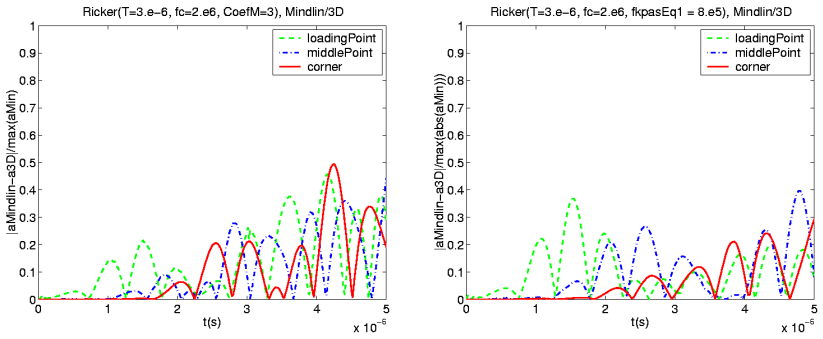

Figure 13. *Gap in accelerations observed at points F, R and S of Mindlin and 3D solutions in the plates with $\beta = 3$ and $\beta = 0.74$*

7. Conclusion

An adaptive finite element approach tailored to modelling the propagation of elastic waves is presented. Membrane and bending wave propagations in plates and shells, generation of shock waves under moving loads are considered by this method with efficiency. The pertinence of Kirchhroff-Love and Mindlin kinematical models with respect to frequency ranges and plate/shell thickness is discussed. A parameter relevant to decide between these shell models is defined; it allows defining the valid frequency domain for the Kirchhoff-Love model. It will be interesting to generalize this result to other shell kinematics models. As for the comparison between the Mindlin and 3D kinematics, the problem is still open: relevant parameters should be found out and the effect of boundary conditions on the wave propagation should be analysed. Fortunately, our first investigation gives some degree of confidence in the Mindlin modelling, as far as the 3D modelling is very expensive and often impossible for engineering structures. The use of enriched shell modelling would probably be a good solution to avoid the full 3D modelling.

8. References

Aubry D., Lucas D., Tie B., « A unified approach to adaptive computations », *European J. for F.E. Methods*, 7(1-2-3), 1997, pp. 105-118.

Aubry D., Lucas D., Tie B., « Adaptive strategy for transient/coupled problems, applications to thermo-elasticity and elasto-dynamics », *Comp. Meth. Appl. Mech. Engrg.*, 176, 1999 pp. 41-50.

Aubry D., Jay G., Tie B., « A combined mesh and model adaptive strategy for the numerical modelling of the ductile damage in thin panels », accepted for publication in *Comp. Meth. Appl. Mech. Engrg.*, 2003.

Babuska I., Rheinboldt W.C., « *A posteriori* error estimates for finite element methods », *SIAM J. Numer. Anal.*, Vol. 15. No. 4, 1978, pp. 736-754.

Bank R.E., Smith R.K., « *A posteriori* error estimates based on hierarchical bases », *Industrial and Applied Mathematics*, 30, 1992, pp. 921-935.

Doyle J.-F., *Wave Propagation in structures, spectral analysis using fast discrete Fourier transforms*, Second Edition, Springer, 1997.

Eringen, Suhubi, *Elastodynamics*, Academic Press, 1975.

Hulbert M., Hughes T.J.R., « Space-time finite element methods for elastodynamics: formulations and error estimates », *Comp. Meth. Appl. Mech. Engrg.*, 66, 1988, pp. 339-363.

Ladevèze P., « Error estimate procedure in the finite element method and application », *J. Num. Anal.*, 3(20), 1983, pp. 485-509.

Ladislav Fryba, *Vibration of solids and structures under moving loads*, Thomas Telford, third edition, 1999.

Leclère J.-L., *Parallel modelling of wave propagation in structures by adaptive finite elements*, PhD thesis, Ecole Centrale Paris, France, 2001.

Johnson C., Hansbo P., « Adaptive finite elements methods in computational mechanics », *Comp. Meth. Appl. Mech. Engrg.*, 101, 1992, pp. 143-181.

Oden J.T., Demkowicz L., Rachkowick W., Westermann T.A., « Toward a universal *h-p* adaptive element strategy: *A posteriori* error estimates based on hierarchical bases », *Comp. Meth. Appl. Mech. Engrg.*, 77, 1989, pp. 113-180.

Tie B., *Adaptive and hierarchical finite elements for elasto-plasticity. Strain localization*, PhD thesis, Ecole Centrale Paris, France, 1993.

Wiberg N.E., Li X., « Implementation and adaptivity of a space-time finite element method for structural dynamics », *Comp. Meth. Appl. Mech. Engrg.*, 156, 1998, pp. 211-229.

Zienkiewich O.C., Zhu J.Z., « The superconvergent patch recovery and *a posteriori* error estimates », *Int. J. Num. Meth. Engng*, 33, 1992, pp. 1331-1382.